

## **CERTIFICATE**

It is certified that the work contained in the thesis titled " **SYNTHESIS AND STUDY OF MAGNETIC AND MAGNETO-TRANSPORT PROPERTIES OF SOME TOPOLOGICAL INSULATORS** "by " **ABHISHEK SINGH** " has been carried out under my/our supervision and that this work has not been submitted elsewhere for a degree. It is further certified that the student has fulfilled all the requirements of Comprehensive Examination, Candidacy and SOTA for the award of Ph.D. Degree.

**Supervisor**  
**(Prof. Sandip Chatterjee)**

### **DECLARATION BY THE CANDIDATE**

I, **ABHISHEK SINGH**, certify that the work embodied in this thesis is my own bonafide work and carried out by me under the supervision of **PROF. SANDIP CHATTERJEE** from **SEPTEMBER, 2012** to **MARCH, 2018**, at the **DEPARTMENT OF PHYSICS**, Indian Institute of Technology (BHU), Varanasi. The matter embodied in this thesis has not been submitted for the award of any other degree/diploma. I declare that I have faithfully acknowledged and given credits to the research workers wherever their works have been cited in my work in this thesis. I further declare that I have not willfully copied any other's work, paragraphs, text, data, results, etc., reported in journals, books, magazines, reports, dissertations, theses, etc., or available at websites and have not included them in this thesis and have not cited as my own work.

Date:

Signature of the Student

Place:

**(ABHISHEK SINGH)**

### **CERTIFICATE BY THE SUPERVISOR(S)**

It is certified that the above statement made by the student is correct to the best of my/our knowledge.

Supervisor

(Prof. Sandip Chatterjee)

Signature of Head of Department

## **COPYRIGHT TRANSFER CERTIFICATE**

**Title of the Thesis: Synthesis and Study of Magnetic and Magneto- Transport Properties of Some Topological Insulators**

**Name of the Student: Abhishek Singh**

### **Copyright Transfer**

**The undersigned hereby assigns to the Indian Institute of Technology (Banaras Hindu University) Varanasi all rights under copyright that may exist in and for the above thesis submitted for the award of the DOCTOR OF PHILOSOPHY.**

Date:

Signature of the Student

Place:

**(ABHISHEK SINGH)**

**Note: However, the author may reproduce or authorize others to reproduce material extracted verbatim from the thesis or derivative of the thesis for author's personal use provided that the source and the Institute's copyright notice are indicated.**



# **CHAPTER-1**

## **Introduction and Literature Review**





## **CHAPTER-2**


### **Experimental: Synthesis Procedure and Characterization Details**






**CHAPTER-3**  
**Magnetic and Magneto-Transport Study**  
**of  $\text{Bi}_2\text{Cu}_x\text{Te}_{3-x}$  ( $x=0, 0.03, 0.09$ )**  
**Topological Insulators**





# CHAPTER-4

## Tuning of Carrier Type, Enhancement of Magnetoresistance and Room Temperature Ferromagnetism in Cu doped $\text{Bi}_2\text{Te}_3$ Topological Insulators

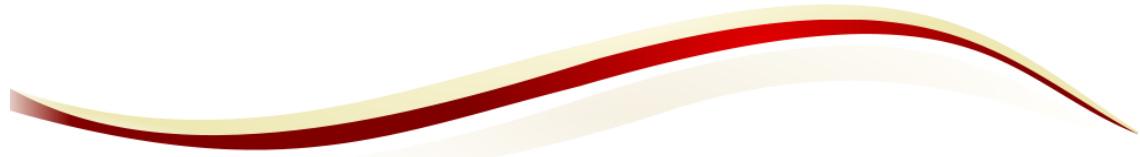


**Abhishek Singh**, R. Singh, T. Patel, G. Okram, A. Lakhani, V. Ganeshan, A. Ghosh, S. Jha, S. Patil, and S. Chatterjee, “Tuning of carrier type, enhancement of Linear magnetoresistance and inducing ferromagnetism at room temperature with Cu doping in  $\text{Bi}_2\text{Te}_3$  Topological Insulators,” *Materials Research Bulletin*, vol. 98, pp. 1-7, 2018.



## CHAPTER-5

# Enhancement in Power Factor due to Anti-Correlation between Electrical Conductivity and Thermoelectric Power and Induced Magnetic Ordering in High Mobility Zn Doped $\text{Bi}_2\text{Te}_3$ Topological Insulator



**Abhishek Singh**, P. Shahi, A. Ghosh, J. Cheng, and S. Chatterjee, “Enhancement in power factor due to anti-correlation between electrical conductivity and thermoelectric power and induced magnetic ordering in high mobility Zn doped  $\text{Bi}_2\text{Te}_3$  topological insulator,” *Journal of Alloys and Compounds*, vol. 731, pp. 297-302, 2018.





## **CHAPTER-6**

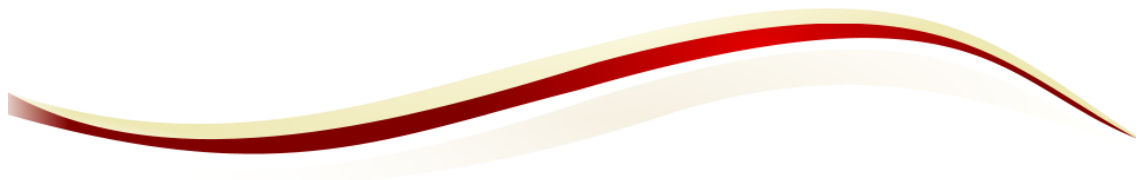
# **Distinguishing Bulk State from Surface State by Simultaneous SdH and dHvA Oscillations in $\text{Sb}_{1.90}\text{Cu}_{0.10}\text{Te}_3$ Topological Insulator**





## CHAPTER-7

# Antiferromagnetic Ordering at Room Temperature in Co-Doped $\text{Sb}_2\text{Te}_3$ Topological Insulators



**Abhishek Singh**, A. Ghosh, and S. Chatterjee, “Antiferromagnetic Ordering at Room Temperature in Co-Doped  $\text{Sb}_2\text{Te}_3$  Topological Insulators,” *Journal of Superconductivity and Novel Magnetism*, vol. 31, no. 2, pp. 299-305, 2018



# **CHAPTER-8**

## **Conclusion and Future Scope**



*Dedicated*

*To*

*My Beloved Parents*

*And My Preceptor*

---

---

**LIST OF FIGURES**

---

---

		<b>Page No.</b>
<b>Chapter 1</b>	<b>Introduction and Literature Review</b>	
Fig. 1.1	Schematic band diagram for metal, semiconductor and insulator	3
Fig.1.2	(a) Schematic representation of topology showing smooth deformation from cup to donut (b) Sphere showing different topology than cup and donut (c) Effect of external parameter on topology of donut	4
Fig.1.3	Schematic diagram of Hall Effect	10
Fig.1.4	Energy band diagram for electrons vs. wave vector for different Landau levels in 3D system	12
Fig.1.5	Schematic representation of Density of state vs. energy of electrons in 3D in presence of applied magnetic field	13
Fig.1.6	Schematic representation of Density of state vs. energy of 2D electron gas in presence of applied magnetic field	15
Fig.1.7	Schematic diagram of quantum Hall Effect	16
Fig. 1.8	Cyclotron orbits (in the bulk) and skipping orbits (at the edges) in the 2D electron system in the presence of applied magnetic field	17
Fig.1.9	(a) Schematic diagram of quantum spin hall Effect, opposite spins propagating in opposite directions (b) Insulating state with a band gap separating occupied and unoccupied state (c) Bulk is insulating but skipping orbits at the edges permits the conduction of electron giving rise to the conducting edge i.e. zero band gap (c) both type of left and right moving path having opposite spins is allowed in QSHE which is protected due to time reversal symmetry (e) At the surface, propagation in any direction is possible, electrons at the surfaces show linear energy momentum relation and hence show Dirac cone in 3D	20

Fig.1.10	Schematic diagram of (a) ordinary Hall Effect showing linear behavior between hall coefficient vs. applied field (b) Quantum anomalous Hall Effect (QAHE) showing hysteresis in the graph of hall coefficient vs. applied field.	23
Fig.1.11	Schematic diagram of weak antilocalization (WAL), black dots represents the scattering centre and red lines are showing the direction of propagation of electrons	24
Fig.1.12	Band structure of Graphene at low energy introduced by Kane and Mele	26
Fig.1.13	Schematic diagram for CdTe/HgTe/CdTe heterostructure (b) Upper Fig. showing bulk energy bands for HgTe and CdTe at $\Gamma$ point, lower Fig. showing CdTe/HgTe/CdTe quantum well in normal regime $d < d_c$ and inverted regime $d > d_c$	28
Fig1.14	(a) Band gap and band offset diagram for asymmetric AlSb/InAs/GaSb quantum wells. The left AlSb barrier layer is connected to a front gate while the right barrier is connected to a back gate. The $E_I$ subband is localized in the InAs layer and $H_1$ is localized in the GaSb layer. Outer AlSb barriers provide an overall confining potential for electron and hole states. (b) Schematic band structure diagram. The dashed line shows the crossing of $E_I$ and $H_1$ in the inverted regime. Hybridization between $E_I$ and $H_1$ , opens the gap.	30
Fig. 1.15	Schematic diagram for valence band and conduction band for SnTe and PbTe materials.	32
Fig. 1.16	Schematic diagram for the valence band and conduction band for pure Bi, Sb and $\text{Bi}_{1-x}\text{Sb}_x$	33
Fig. 1.17	Spin resolved ARPES study of the topological insulator surface. (a) Schematic diagram of spin-ARPES measurement setup which was used to measure the spin distribution on the (111) surface Fermi surface of the	34

	sample $\text{Bi}_{0.91}\text{Sb}_{0.09}$ (b) Spin orientations on the surface create a vortex like pattern around $\Gamma$ point. A net Berry phase is extracted from the full Fermi-surface data (c) Net polarizations along $x$ , $y$ , and $z$ directions are shown. $P_z \sim 0$ suggests that spins lie mostly within the surface plane	
Fig. 1.18	(a) ARPES study of $\text{Bi}_{1-x}\text{Sb}_x$ on the (111) surface of $\text{Bi}_{0.9}\text{Sb}_{0.1}$ which probes the occupied surface states as a function of momentum on the line connecting the time reversal invariant points in the surface Brillouin zone. Only the surface bands cross the Fermi energy five times. (b) A schematic diagram of the 3D Brillouin zone and its (111) surface projection.	35 45
Fig. 1.19	(a) Spatially resolved conductance study of the (111) surface obtained at 0 mV over an scanning area of $1000\text{\AA} \times 1000\text{\AA}$ . (b) Spin-ARPES study of the surface state measured at the Fermi level. Arrows are showing about the spin textures from spin ARPES measurements. (c) Fourier transforms scanning tunneling spectroscopy FT-STs at Fermi energy ( $E_F$ ). (d) The joint density of states (JDOS) at Fermi energy ( $E_F$ ). (e) The spin dependent scattering probability (SSP) at Fermi energy ( $E_F$ ). (f) Close up of the JDOS, FT-STs, and SSP at Fermi energy ( $E_F$ ), along the $\Gamma$ - $M$ direction.	36
Fig. 1.20	Band structure of $\text{Sb}_2\text{Se}_3$ , $\text{Sb}_2\text{Te}_3$ , $\text{Bi}_2\text{Se}_3$ and $\text{Sb}_2\text{Te}_3$ calculated by <i>ab initio</i> density functional theory, red represents occupied bulk and surface states and blue the bulk band gap.	37
Fig. 1.21	(a) Crystal structure of $\text{Bi}_2\text{Se}_3$ (b) Brillouin zone of $\text{Bi}_2\text{Se}_3$ , (c) Three possible positions A, B, C in-plane triangle lattice.	39
Fig. 1.22	Schematic representation of the band structure of $\text{Bi}_2\text{Se}_3$ (I) Hybridization of Bi and Se orbitals (II) formation of bonding and anti bonding states due to inversion	41

	symmetry (III) Crystal field splitting (IV) effect of spin orbit coupling.	
Fig. 1.23	ARPES measurement of $\text{Bi}_2\text{Se}_3$ (a, b) cuts along the M- $\Gamma$ -M and K- $\Gamma$ -K directions (c) momentum distribution curve corresponding to (a)	42
Fig. 1.24	(a) ARPES study of $\text{Bi}_2\text{Se}_3$ showing surface electronic states with a single spin polarized Dirac cone. (b) The surface Fermi surface exhibits a chiral left handed spin texture. (c) Surface electronic structure of $\text{Bi}_2\text{Se}_3$ computed in the local density approximation. The shaded regions describe bulk states, and the lines are showing the surface states. (d) Schematic of the spin-polarized surface-state dispersion in $\text{Bi}_2\text{X}_3$ (1;000) topological insulators.	42
Fig. 1.25	ARPES experiment of $\text{Bi}_2\text{Te}_3$ topological insulator, Fig. A to D is presenting the result of doping concentration Sn in to $\text{Bi}_2\text{Te}_3$ from $\delta=0$ to 0.9%. Each section is showing the band dispersion along the K- $\Gamma$ -K direction and the respective momentum distribution curve, here SSB stands for surface state band, BCB- bulk conduction band and BVB- bulk valence band.	43
Fig. 1.26	Magnetic impurity such as Fe on the surface of $\text{Bi}_2\text{Se}_3$ opens a gap at the Dirac point. The interaction of Fe ions with the Se surface set a band gap and the time reversal symmetry breaking disorder potential introduced on the surface. (b) A comparison of surface band dispersion with and without Fe doping. (C) and (d) Nonmagnetic disorder created via molecular absorbent $\text{NO}_2$ or alkali atom adsorption K or Na on the surface leaves the Dirac node intact in both $\text{Bi}_2\text{Se}_3$ and $\text{Bi}_2\text{Te}_3$ .	44
Fig. 1.27	Variation of Magnetization vs applied magnetic field for samples $\text{Bi}_{2-x}\text{Fe}_x\text{Te}_3$ ( $x=0, 0.08, 0.15, 0.20, 0.25$ and $0.30$ ) (b) variation of electrical resistivity vs temperature for samples $\text{Bi}_{2-x}\text{Fe}_x\text{Te}_3$ ( $x=0, 0.08, 0.15, 0.20, 0.25$ and $0.30$ )	45



	Inset shows the zoom pic of resistivity below 20K.	
Fig. 1.28	(a) Variation of electrical resistivity vs. temperature for samples $\text{Bi}_{2-x}\text{Mn}_x\text{Te}_3$ ( $x=0, 0.03, 0.05, 0.09$ and $0.15$ ), Inset shows the seebeck coefficient of sample ( $x=0.03$ and $0.15$ ) (b) variation of Magnetization vs. applied magnetic field for samples $x=0.03$ and $0.15$ , Inset represents the $\chi$ vs. T graph for $x=0.03$ sample (c) variation of electrical resistivity vs. temperature for samples $\text{Bi}_{2-x}\text{Ca}_x\text{Se}_3$ ( $x=0, 0.005$ and $0.012$ ), Inset shows the normalized resistivity.	46
Fig. 1.29	(a) Variation of MR as a function of applied magnetic field (H); Inset shows the MR ratio between 3K-340K for $\text{Bi}_2\text{Te}_3$ nanosheets (b) Variation of MR as a function of applied magnetic field showing linear behavior in $\text{Bi}_2\text{Te}_3$ film (c) Plot of Hall mobility and MR showing good agreement with PL model in $\text{Bi}_2\text{Te}_3$ film (d) SdH oscillations in $\text{Bi}_2\text{Se}_{2.1}\text{Te}_{0.9}$	48
Fig. 1.30	(a) Variation of resistivity vs. temperature for $\text{Bi}_2\text{Te}_3$ sample showing superconductivity ( $T_c$ )~ 2.7K (b) Variation of resistivity vs. temperature for $\text{Bi}_2\text{Te}_3$ sample showing superconductivity ( $T_c$ )~ 8K (c) Variation of resistivity vs. temperature for $\text{Bi}_2\text{Te}_3$ sample showing superconductivity ( $T_c$ )~ 9K (d) Variation of resistivity vs. temperature for $\text{Cu}_{0.12}\text{Bi}_2\text{Se}_3$ sample showing superconductivity ( $T_c$ )~ 3.8K.	49
<b>Chapter 2</b>	<b>Experimental: Synthesis Procedure and Characterization details</b>	
Fig.2.1	(a) Mechanism and (b) experimental set up of XRD instrument.	53
Fig.2.2	Schematic diagram of test circuit for measuring resistivity with the four-point probe method.	55
Fig.2.3	Schematic diagram for Hall Effect measurement	56
Fig.2.4	Schematic diagram for thermoelectric measurement	58
Fig.2.5	Schematic diagram of X-ray photoemission spectroscopy	59

Fig.2.6	(a) $2\omega$ detection principle.(b) SQUID detection schematic. (c) MPMS instrument set up used for characterization	61
Fig. 2.7	Schematic diagram of SQUID magnet	63
Fig. 2.8	Microscope (SEM) (b) Instrumental set up for the SEM instrument using for the characterization.	65
Fig.2.9	(a)Principle of Atomic Force Microscopy (AFM) (b) instrumental Set up of AFM used for characterization	67
<b>Chapter 3</b>	<b>Magnetic and Magneto-transport study of <math>\text{Bi}_2\text{Cu}_x\text{Te}_{3-x}</math> (<math>x=0, 0.03, 0.09</math>) Topological Insulators</b>	
Fig.3.1	(a)XRD pattern of as prepared $\text{Bi}_2\text{Cu}_x\text{Te}_{3-x}$ ( $x=0, 0.03,$ $0.09$ ) (b) Zoom portion of (00 15) peak, (c) Variation of lattice parameter $c$ as a function of doping concentration $x$ .	71
Fig.3.2	Laue pattern of the single crystals $\text{Bi}_2\text{Cu}_x\text{Te}_{3-x}$ ( $x=0, 0.03,$ $0.09$ ).	72
Fig.3.3	Variation of resistivity as a function of temperature at different magnetic field for the samples $\text{Bi}_2\text{Cu}_x\text{Te}_{3-x}$ ( $x=0,$ $0.03, 0.09$ )	73
Fig.3.4	(a, b, c) Variation of Hall resistivity with applied magnetic field at different temperatures for the samples $\text{Bi}_2\text{Cu}_x\text{Te}_{3-x}$ ( $x=0, 0.03, 0.09$ ) respectively, Inset I is showing variation of carrier concentration as a function of temperature whereas Inset II is showing variation of carrier mobility with temperature at different applied magnetic field for respective samples.	75
Fig.3.5	(a, b, c) Variation of magnetoresistance as a function of applied magnetic field under different temperatures for the samples $x=0, 0.03$ and $0.09$ respectively.	78
Fig.3.6	Study of SdH oscillation for the sample $x=0.03$ (a) SdH oscillations plotted against $1/B$ at different temperatures. (b) SdH oscillations and Landau levels with inverse magnetic field and linear fitted curve (red line). (c) The FFT corresponding to Fig. (a); (d) Fit to the Dingle damping term at 2K with the resulting Dingle temperature	79

	$T_D=9K$ , Inset show the L-K fitting of the SdH oscillation and obtained cyclotron mass ( $m_c$ ) $0.13 m_e$ from fitting, at applied field $8.74T$	
Fig.3.7	Study of SdH oscillation for the sample $x=0.09$ (a) SdH oscillations plotted against $1/B$ at different temperatures. (b) SdH oscillations and Landau levels with inverse magnetic field and linear fitted curve (red line). (c) The FFT corresponding to Fig. (a); (d) Fit to the Dingle damping term at $2K$ with the resulting Dingle temperature $T_D=13K$ , Inset show the L-K fitting of the SdH oscillation and obtained cyclotron mass ( $m_c$ ) $0.18 m_e$ from fitting, at applied field $10.74T$ .	83
Fig.3.8	Susceptibility ( $\chi$ ) vs. Temperature ( $T$ ) curves at an applied field of $1000 Oe$ for the samples $x=0.03$ and $0.09$ . Figs. (b and c) showing individual fitted curves for the samples $x=0.03$ and $0.09$ .	85
Fig.3.9	M-H curves at $2K$ for the samples $x=0.03$ and $0.09$ .	87
<b>Chapter 4</b>	<b>Tuning of Carrier type, Enhancement of Magnetoresistance and Room Temperature Ferromagnetism in Cu doped <math>Bi_2Te_3</math> Topological Insulators</b>	
Fig.4.1	Room temperature X-ray diffraction patterns of $Bi_2Te_3$ and $Bi_2Cu_{0.15}Te_{2.85}$ , Inset: Laue pattern of $Bi_2Cu_{0.15}Te_{2.85}$ .	91
Fig.4.2	(a, b) Valence Band studies of $Bi_2Te_3$ and $Bi_2Cu_{0.15}Te_{2.85}$ by Angle Integrated Photoemission Spectroscopy.	93
Fig.4.3	Temperature dependence of electrical resistivity for $Bi_2Te_3$ and $Bi_2Cu_{0.15}Te_{2.85}$ and (b) Variation of Seebeck coefficient as a function of temperature. Inset represents the power factor (PF) of the $Bi_2Te_3$ and $Bi_2Cu_{0.15}Te_{2.85}$ .	95
Fig.4.4	(a) Magnetic field dependence of the Hall resistivity of the $Bi_2Te_3$ at $200K$ and $300K$ . Inset I represents the variation of carrier concentration as a function of temperature whereas Inset II shows the variation of carrier mobility	97

	with temperature for $\text{Bi}_2\text{Te}_3$ and (b) Magnetic field dependence of the Hall resistivity of the $\text{Bi}_2\text{Cu}_{0.15}\text{Te}_{2.85}$ at 200K and 300K, Inset is the variation of carrier mobility as a function of applied magnetic field at 200K and 300K.	
Fig.4.5	(a) Magnetoresistance as a function of magnetic field for $\text{Bi}_2\text{Te}_3$ at different temperatures and (b, c, d) Magnetoresistance as a function of magnetic field for $\text{Bi}_2\text{Cu}_{0.15}\text{Te}_{2.85}$ at different temperatures.	101
Fig.4.6	(a)-(b) Field dependence of magnetization for $\text{Bi}_2\text{Te}_3$ and $\text{Bi}_2\text{Cu}_{0.15}\text{Te}_{2.85}$ samples at 5K and 50K respectively. The inset represents hysteresis in $\text{Bi}_2\text{Cu}_{0.15}\text{Te}_{2.85}$ sample.(c)Temperature dependence of magnetization for $\text{Bi}_2\text{Cu}_{0.15}\text{Te}_{2.85}$ at an applied magnetic field of 1000 Oe showing ferromagnetic nature.(d) Field dependence of magnetization for $\text{Bi}_2\text{Cu}_{0.15}\text{Te}_{2.85}$ at different temperatures (i.e. 2K, 5K 50K and 300K).	104
Fig.4.7	X-ray Photoemission core level spectrum of Bi and Te in $\text{Bi}_2\text{Te}_3$ sample (a) & (b) whereas (c), (d)&(e) show core level spectrum of Bi, Te and Cu in $\text{Bi}_2\text{Cu}_{0.15}\text{Te}_{2.85}$ .	106
<b>Chapter 5</b>	<b>Enhancement in power factor due to anti-correlation between Electrical Conductivity and Thermoelectric power and Induced magnetic ordering in high mobility Zn doped <math>\text{Bi}_2\text{Te}_3</math> Topological Insulator</b>	
Fig.5.1	(a)Room temperature X-ray diffraction patterns of $\text{Bi}_{2-x}\text{Zn}_x\text{Te}_3$ ( $x=0, 0.10, 0.20$ ) single crystals, (b) Variation of lattice parameter with Zn concentration for $\text{Bi}_{2-x}\text{Zn}_x\text{Te}_3$ ( $x=0, 0.10, 0.20$ ).	111
Fig.5.2	Temperature dependence of zero field electrical resistivity for $\text{Bi}_{2-x}\text{Zn}_x\text{Te}_3$ samples ( $X=0, 0.10, 0.20$ ) and Inset I is showing the field dependence of magnetization (MH) for $\text{Bi}_{2-x}\text{Zn}_x\text{Te}_3$ ( $X=0.10$ and $0.20$ ) samples, Inset II is showing magnetization vs. temperature (MT) curve for $X=0.10$ sample and Inset III is showing MH curve for	113

	X=0.10 sample at different temperatures <i>viz.</i> 2K, 18K, 56K, 300K.	
Fig.5.3	Variation of power factor (PF) as a function of temperature for $\text{Bi}_{2-x}\text{Zn}_x\text{Te}_3$ . Inset: represents the thermopower of the $\text{Bi}_{2-x}\text{Zn}_x\text{Te}_3$ .	115
Fig.5.4	(a) Magnetic field dependence of the Hall resistivity at different temperatures for $\text{Bi}_2\text{Te}_3$ . (b) Magnetic field dependence of the Hall resistivity at different temperatures for x=0.20 sample. Inset: Variation of mobility as a function of temperature for $\text{Bi}_{2-x}\text{Zn}_x\text{Te}_3$ (x=0, 0.10, 0.20).	116
Fig.5.5	(a, b, c) Normalized MR as a function of magnetic field at different temperatures $\text{Bi}_{2-x}\text{Zn}_x\text{Te}_3$ (x=0, 0.10, 0.20). (d) Variation of mobility and MR as a function of temperature for the sample x=0.20 at low field. Inset: Variation of MR at 2K for $\text{Bi}_{2-x}\text{Zn}_x\text{Te}_3$ (x=0, 0.10, 0.20)	119
<b>Chapter 6</b>	<b>Distinguishing Bulk state from Surface state by simultaneous SdH and dHvA oscillations in <math>\text{Sb}_{1.90}\text{Cu}_{0.10}\text{Te}_3</math> Topological Insulator</b>	
Fig.6.1	Magnetic field dependence of the Hall resistivity of $\text{Sb}_{1.90}\text{Cu}_{0.10}\text{Te}_3$ at different temperatures. Inset (a) represents the variation of carrier mobility as a function of temperature, Inset (b) Magnetic field dependence of the Hall mobility at 1.8K and 300K.	127
Fig.6.2	(a)Magnetoresistance as a function of magnetic field of $\text{Sb}_{1.90}\text{Cu}_{0.10}\text{Te}_3$ at different temperatures. Inset: variation of electrical resistivity with respect to Temperature. (b) SdH oscillations of the longitudinal resistance (second derivative) with 1/B at different temperatures. (c) The FFT corresponding to Fig. (b); (d) SdH oscillations (second derivative) and Landau levels with inverse magnetic field and linear fitted curve (red line).	129
Fig.6.3	Fit to the Dingle damping term at 1.8K with the resulting Dingle temperature $T_D=36.8\text{K}$ , Inset show the L-K fitting	131

	of the SdH oscillation and obtained cyclotron mass ( $m_c$ ) from fitting at applied field 7.32T.	
Fig.6.4	Field dependence of magnetization of $Sb_{1.90}Cu_{0.10}Te_3$ at 2K, 5K and 10K respectively. The inset represents Temperature dependence of magnetization in ZFC mode at an applied magnetic field of 1000 Oe. (b) SdH oscillations in the magnetization (second derivative) with $1/B$ at different temperatures. (c) The FFT corresponding to Fig. (b), (d) dHvA oscillations of the magnetization (second derivative) and Landau levels with inverse magnetic field and linearly fitted data red line).	132
Fig.6.5	Fit to the Dingle damping term at 1.8K with the resulting Dingle temperature $T_D=29.3K$ , Inset shows the L-K fitting of the dHvA oscillation in magnetization and obtained cyclotron mass ( $m_{cyc}$ ) from fitting at applied field 5.52T.	133
<b>Chapter 7</b>	<b>Presence of Anti-Ferromagnetic ordering at Room Temperature in low concentration Co doped <math>Sb_2Te_3</math> Topological Insulators</b>	
Fig.7.1	X-ray diffraction (XRD) pattern of $Sb_{2-x}Co_xTe_3$ ( $x=0, 0.02, 0.06, 0.10$ ) single crystals.	139
Fig.7.2	Le Bail refinement of the XRD pattern for the samples ( $x=0, 0.02, 0.06, 0.10$ ).	140
Fig.7.3	(a, b) Represents the EDX spectra of the samples $x=0$ and $x=0.10$ respectively.	141
Fig.7.4	(a, b) Show the SEM images of the samples $x=0$ and $x=0.10$ respectively. (c, d) Represents the 3D AFM images of $x=0$ and $x=0.10$ samples respectively, (e) shows the variation of height vs. scanned distance for $x=0$ sample.	142
Fig.7.5	Represents the XPS survey scan of $x=0.10$ sample, Inset: XPS high resolution core level spectra of Co region (2p).	144
Fig.7.6	Shows the variation of magnetization (M) vs. temperature (T) for the Co doped samples ( $x= 0.02, 0.06, 0.10$ ).	146

(a, b, c) show the variation of magnetization (M) vs. applied field (H) for the Co doped samples ( $x= 0.02, 0.06, 0.10$ ) respectively. Inset of Fig.7.7 (a), (b) and (c) represents the zoom picture of MH behavior at 2K. Fig. 7.7 (d) represents compile picture of M vs. H behavior for the samples ( $x= 0.02, 0.06, 0.10$ ) at 2K, Inset (I): shows the compile picture of M vs. H for the samples ( $x= 0.02, 0.06, 0.10$ ) at 300K, Inset (II) represents the variation of coersive field ( $H_C$ ) as a function of Temperature (T) for the samples  $x=0.02$  and  $x=0.06$ .

---

---

***LIST OF TABLES***

---

---

		<b>Page No.</b>
Table 3.1	Different parameters obtained from susceptibility curves of samples $x=0.03$ and $0.09$ .	86
Table 6.1	Different parameters ( $k_F$ , the Fermi momentum; $n_b$ , the bulk carrier concentration; $n_s$ , the surface carrier concentration; $n_{tot}$ , the total carrier concentration) obtained from SdH, dHvA oscillations and their first Fourier transforms.	134
Table 7.1	Different parameters obtained from Le-bail refinement of the samples ( $x=0, 0.02, 0.06, 0.10$ ).	140



Spin-orbit induced topological insulator (TI), a new type of materials, which are insulating in bulk but conducting at the surfaces, has attracted a large interest in the area of condensed matter physics. This is due to the gapless edge or spin resolved surface states (SS), which are topologically protected by time reversal symmetry (TRS). The spins are locked in the perpendicular direction of momentum due to the strong spin-orbit interaction. As a matter of fact, electrical conduction is robust against backscattering at the edge states or on the surfaces in TIs. These special helical spin properties of electrons make TIs interesting and relevant for new physics. Since the locking of spin and orbital states is protected by time reversal symmetry, the delocalized surface states are unaffected from nonmagnetic dopants and defects. Moreover the coupling of the spin and orbital angular momentum of an electron leads to an inversion of the band gap. The possibility of Majorana Fermions, topological superconductivity, novel magnetoelectric quantum states, the absence of backscattering from nonmagnetic impurities, exciton condensation, magnetic monopole, and anomalous quantum Hall effect types of exotic properties in TIs are very promising in the application of spintronic devices and quantum computing. Topological surface states in  $\text{Bi}_2\text{Te}_3$  and  $\text{Bi}_2\text{Se}_3$  with only one mass less Dirac cone on each surface were studied using Angle-resolved photoemission spectroscopy (ARPES). Quantum magneto-transport phenomenon such as weak antilocalization, Aharonov-Bohm oscillations and quantum conductance fluctuations are associated with surface states. The time reversal symmetry protection of the Dirac point can be lifted by magnetic dopant, resulting in a band gap due to the separation in the upper and lower branches of the Dirac cone. It has been theoretically predicted that surface state of a topological insulator show a linear energy-

momentum relation similar to Dirac fermions. Such type of backscattering free surface with locked spin and momentum may serve as a platform for both fundamental physics and technological applications like spintronics or quantum computing.

In **Chapter1**, an overview of some of the essential properties of these new types of materials as well as related properties of quantum Hall insulators is given. The purpose of this chapter was to give an introduction to some of the most important properties and to provide information on the analogies and differences between the different systems.

In **Chapter 2**, we have discussed the synthesis process and the different experimental techniques which have been used to characterize the samples. Information about pure phase of the sample was obtained from the X-ray diffraction (XRD). We have investigated transport properties such as electrical resistivity, thermoelectric property, Hall Effect and magnetoresistance (MR) of the samples using PPMS. Variation of magnetization (M) with temperature (T) and applied magnetic field (H) are reported. Surface morphology and chemical states of the constituent elements have been investigated using SEM and XPS analysis. Since we get only 2D image using SEM, for 3D image we used AFM technique also.

In **Chapter 3**, we have investigated structural, resistivity, magneto-transport and magnetic properties of  $\text{Bi}_2\text{Cu}_x\text{Te}_{3-x}$  ( $x=0, 0.03, 0.09$ ) samples. Single crystallinity is further investigated by Laue pattern. It is also observed that Cu doping tunes the carrier from  $n$  to  $p$  type which is attributed due to the  $\text{Te}_{\text{Bi}}$  and  $\text{Bi}_{\text{Te}}$  antisites effects. With Cu doping, resistivity increases which may be due to the extra scattering centers produced due to Cu. Shubnikov-de Hass oscillation has been studied. Quantum anomalous Hall Effect (QAHE) has been observed in Hall analysis of the doped samples which was an indication of magnetic ordering in doped samples. Variation of magnetization (M) with temperature (T) i.e., MT as well as with applied magnetic

field (H) i.e., MH experiment also confirm the presence of ferromagnetism in Cu doped  $\text{Bi}_2\text{Te}_3$  samples.

In **Chapter 4**, structural, resistivity, thermoelectric power, magneto-transport and magnetic properties of  $\text{Bi}_2\text{Cu}_{0.15}\text{Te}_{2.85}$  topological insulators have been investigated. The tuning of charge carriers from *n* to *p* type by Cu doping at Te sites of  $\text{Bi}_2\text{Te}_3$  is observed both from Hall Effect and thermoelectric power measurements. Carrier mobility decreases with the doping of Cu which provides evidence of the movement of Fermi level from bulk conduction band to the bulk valence band. Thermoelectric power also increases with doping of Cu. In present investigation we have found room temperature ferromagnetism in  $x=0.15$  sample. The observed value of MR was as large as 1000% in  $x=0.15$  sample. Presence of QAHE even at 300K was also supporting the presence of ferromagnetism in Cu doped sample.

In **Chapter 5**, electrical resistivity, thermoelectric power, magnetotransport and magnetization of Zn doped  $\text{Bi}_2\text{Te}_3$  Topological Insulator were studied. Electrical conductivity is enhanced at higher Zn concentration, and the carrier mobility estimated from Hall data reaches a remarkable value of  $\sim 7200 \text{ cm}^2 \text{ V}^{-1}\text{S}^{-1}$ . Large positive magnetoresistance (MR $\sim$ 400%) is observed in high mobility samples. Interestingly, it is found that the coupling between electrical conductivity and Seebeck coefficient is broken for higher Zn doped  $\text{Bi}_2\text{Te}_3$  samples which effectively enhances the thermoelectric power factor (from  $2.1 \text{ mW/K}^2\text{m}$  for  $\text{Bi}_2\text{Te}_3$  to  $4.64 \text{ mW/K}^2\text{m}$  for Zn doped  $\text{Bi}_2\text{Te}_3$ ).

In **Chapter 6**, we have investigated the quantum oscillations both from magneto-transport and magnetic measurements in Cu doped  $\text{Sb}_2\text{Te}_3$  sample. From both the Shubnikov–de Haas (SdH) and the de-Haas van Alphen (dHvA) oscillations the bulk and surface states in TI can be distinguished without any angle dependent measurements. In the present chapter, the

magneto-transport and magnetization measurements of  $\text{Sb}_{1.90}\text{Cu}_{0.10}\text{Te}_3$  were performed at different temperatures and different fields. Magneto-transport measurement at high field indicates the coexistence of both bulk and surface states whereas magnetization study at high field shows the existence of bulk state. Lifshitz-Kosevich and first Fourier transform (FFT) analysis supports the signature of bulk and surface states.

In **chapter 7**, structural and magnetic properties of Co doped  $\text{Sb}_2\text{Te}_3$  topological insulators have been investigated. Surface morphology has been studied using scanning electron microscope (SEM) and atomic force microscope (AFM). X-ray photo electron spectroscopy (XPS) study reveals the mixed states of Co in  $\text{Co}^{2+}$  and  $\text{Co}^{3+}$ . Magnetic study indicates that the substitution of Co in  $\text{Sb}_2\text{Te}_3$  not only tune the materials from diamagnetic to antiferromagnetic (even at room temperature) but also propose a promising materials for antiferromagnetic TI which may be useful even for room temperature applications.

In **chapter 8**, we have discussed conclusion of entire thesis along with the future prospective of our work.